Face Centred Cubic Multi-Component Equiatomic Solid Solutions in the Au-Cu-Ni-Pd-Pt System

Jens Freudenberger [1,2,*], David Rafaja [2], David Geissler [1], Lars Giebeler [1], Christiane Ullrich [2], Alexander Kauffmann [3], Martin Heilmaier [3] and Kornelius Nielsch [1,4]

[1]   Leibniz Institute for Solid State and Materials Research Dresden (IFW Dresden), Helmholtzstr. 20, 01069 Dresden, Germany; d.geissler@ifw-dresden.de (D.G.); l.giebeler@ifw-dresden.de (L.G.); k.nielsch@ifw-dresden.de (K.N.)
[2]   TU Bergakademie Freiberg, Institute of Materials Science, Gustav-Zeuner-Str. 5, 09596 Freiberg, Germany; rafaja@ww.tu-freiberg.de (D.R.); christiane.ullrich@ww.tu-freiberg.de (C.U.)
[3]   Karlsruhe Institute of Technology (KIT), Institute for Applied Materials (IAM-WK), Engelbert-Arnold-Str. 4, 76131 Karlsruhe, Germany; alexander.kauffmann@kit.edu (A.K.); martin.heilmaier@kit.edu (M.H.)
[4]   TU Dresden, Institute of Materials Science, 01062 Dresden, Germany
*   Correspondence: j.freudenberger@ifw-dresden.de; Tel.: +49-351-4659-550

Abstract: A single-phase solid solution is observed in quaternary and quinary alloys obtained from gold, copper, nickel, palladium and platinum. The lattice parameters of the alloys follow the linear rule of mixture when considering the lattice parameters of the elements and their concentration. The elements are a priori not homogeneously distributed within the respective alloys resulting in segregations. These segregations cause a large broadening of X-ray lines, which is accessed in the present article. This correlation is visualized by the help of local element mappings utilizing scanning electron microscopy including energy dispersive X-ray analysis and their quantitative analysis.

1. Introduction

Recently, the investigation of the physical, structural and mechanical properties of multi-component solid solutions was fostered by the discovery of a new materials class consisting of equiatomic concentrations of at least five components, named high entropy alloys. The so-called Cantor alloy, CoCrFeMnNi, which was discovered as the first of its kind in 2004, unexpectedly exhibited a single phase [1]. Until then, the common approach in alloy design was focused on one principal element forming the matrix and additional alloying elements, for which reason the families of the alloys were named after the matrix element. If there were more elements with a major concentration, no matrix element can be identified. It was generally accepted in physical metallurgy that increasing the number of elements in an alloy most likely favors the formation of intermetallic phases and complex microstructures or even promotes the freezing of amorphous liquids, yielding eventually metallic glasses [2,3]. Multi-component equiatomic solid solutions as, e.g., the Cantor alloy, do not fall into these categories. It was Yeh et al. who proposed that a concentrated solid solution may be stabilized by the large configurational entropy of mixing ΔS_{config} [4]. This ΔS_{config} is maximum for an equiatomic composition and can be calculated as:

$$\Delta S_{\text{config}} = -R \cdot \sum_i x_i \ln(x_i) \tag{1}$$

Herein, R is the ideal gas constant and x_i the concentration of the respective element. For an equiatomic solid solution with five elements, S_{config} amounts to 13.38 J/(K·mol), while, e.g., for the commercially-applied aluminum alloy 6061 (also with five elements involved: Al97.9Cu0.3Mg1Si0.6Cr0.2), the configurational entropy is only 0.94 J/(K·mol). From Equation (1), it can be deduced that, in general, S_{config} of equiatomic alloys increases with increasing number of elements in the alloy. Thus, high entropy alloys are defined as solid solutions with at least five elements whose individual concentrations may range between 5 and 35 at.%. However, present views on this new material class have shown that the large configurational entropy is neither sufficient nor necessary to form multi-component solid solutions [3,5–7], but the name of the family was established.

Presently, there are only a few truly single-phase high entropy alloys known [8], i.e., CoCrFeMnNi (fcc) [1], AlLiMgScTi (fcc) [9], AlCoCrFeNi (bcc) [10], HfNbTaTiZr (bcc) [11], MoNbTaVW (bcc) [12] and DyGdHoTbY (hcp) [13]. The latter three are noteworthy, since the solid solution is observed within the complete concentration range for the known binary and ternary systems formed upon these elements. This suggests that the high entropy alloy is not limited to a narrow range near the equiatomic composition. With this article, a new multi-component equiatomic solid solution is published: AuCuNiPdPt. This high entropy alloy is unique in the sense that all single components and the solid solution in the whole concentration range are characterized by the Cu-type fcc structure. Therefore, this solid solution is expected to enable the study of the effect of alloying elements on materials' properties in a wide range of concentrations. The known binary and ternary phase diagrams built from Au, Cu, Ni, Pd and Pt show a homogeneous solid solution at least at high temperatures. Hence, primary solidification yields to a single-phase solid solution. In some cases, this solid solution may be decomposed into two phases at moderate temperatures as, e.g., Au-Ni [14].

2. Outline

The purpose of the present article is two-fold: (i) to provide an experimental verification of the Cu-type fcc phase for all investigated compositions by investigating the (near) equiatomic quinary and quaternary compositions and (ii) to provide a sound analysis of the impact of segregations and lattice strain on the X-ray diffraction (XRD) line-broadening in an artificially-segregated alloy.

The Au-Cu-Ni-Pd-Pt system was chosen, as the alloys are single-phase and as the AuCuNiPdPt alloy might be used as a benchmark for high entropy alloys to cleanly separate the material behavior of the high entropy alloy from that of conventional single-phase alloys without the necessity to consider secondary phases. Therefore, this system might be used in the future to identify which issues are special for high entropy alloys leading to their peculiar properties.

The large broadening of X-ray lines is interpreted in terms of segregations, which appear already in the as-cast state and are artificially promoted. Among the artificially-segregated alloys under investigation, AuCuNiPt shows the largest line-width of the X-ray reflections. For this reason, this system was chosen for further investigation. The comparison of the segregated and the homogenized states of AuCuNiPt was used to separate the impact of segregations and local lattice strains on the line-broadening. The in-depth investigations of the segregations is done by XRD experiments and scanning electron microscopy (SEM), including energy dispersive X-ray analysis (EDX). The microstructural analysis provides the origin of the large observed line-broadening of XRD lines. This should also be of relevance for other near equiatomic multi-component solid solutions, as they typically also show large line widths in X-ray diffraction experiments [1,6,15].

3. Materials and Methods

Polycrystalline samples of quaternary and quinternary solid solutions were prepared from pure elements (purity of 99.9% or higher), namely gold, copper, nickel, palladium and platinum, in equimolar composition. The metals were melted in an arc furnace on a water-cooled copper plate under argon atmosphere (400 mbar). In order to achieve an improved homogeneity, the samples were re-melted three times and turned over between the individual melting steps. Nevertheless,

small deviations from the intended composition occurred, as determined on a large scale by energy dispersive X-ray analysis and inductively coupled plasma optical emission spectrometry (OPTIMA 4300DV, Perkin-Elmer, Waltham, MA, USA). For this reason the nominal composition of the resulting alloys are given in this article. Subsequently to melting, the samples were heat treated for homogenization at 1000 °C for 24 h. In order to investigate the effect of segregations, samples were further heat treated in the two-phase region (solid solution + liquid). For both heat treatments, the samples were placed in sealed quartz tubes, which were evacuated three times to a pressure below 1×10^{-3} mbar and re-filled with Ar to ambient pressure for the initial and to a pressure of 300 mbar for the last evacuation and re-filling cycle. After the argon atmosphere in the tubes has been set, the quartz tubes were sealed.

In order to reveal (i) phase purity and (ii) the crystal structure of the present phases, XRD experiments were performed. For this purpose, parts of the samples were crushed to powders and glued to glass substrates with the help of a thin layer of silicone grease which does not show any reflection in the XRD patterns, only a slight increase of the background signal. The XRD experiments were performed on a Philips PW3050 diffractometer (Almelo, The Netherlands) in Bragg-Brentano geometry operated at 40 kV and 40 mA, using CoK$_\alpha$ radiation. The scans were taken in the range of $2\Theta = 20°$ to $140°$ in steps of $\Delta 2\Theta = 0.02°$ with a scanning velocity of 10 s per step. The sample spun during measurement at one turn per second. The receiving slit was fixed to $1°$ and a mask was used to limit the beam to the area that was covered with powder, i.e., a region with 1 cm in diameter.

The analysis of the XRD patterns confirmed the single-phase nature of the samples and the presence of the fcc crystal structure (space group $Fm\bar{3}m$, # 225). The Rietveld analysis was done for the Cu structure type with the help of the FULLPROF code [16,17]. The atoms were placed on the Wyckoff positions 4*a* (0,0,0) with an occupancy according to the stoichiometry. The instrumental broadening of the diffractometer was determined upon a measurement of LaB$_6$ standard and the gained instrumental resolution function was used for the Rietveld analysis. The Rietveld analysis involved the sample displacement, the lattice parameter, the overall isotropic temperature factor, as well as two profile parameters describing the contribution of the small crystallite size and the variation of the interplanar spacing to the XRD line broadening. The Rietveld analysis was restricted to these parameters. It predominantly aims at the determination of the lattice parameter. Furthermore, the number of independent parameters was adjusted to the number of reflections.

For microstructural investigations the samples were prepared by conventional metallographic procedures. Subsequent to grinding the samples were polished successively with 3 μm diamond, 1 μm diamond and Mastermet 2 suspension. Microstructural characterization was performed by scanning electron microscopy (SEM) using a FEI Helios Nanolab 600i operated at an acceleration voltage of 20 kV. The probe current was set to 11 nA for imaging. In addition, energy dispersive X-ray analysis (EDX) was performed utilizing an EDAX Genesis system (EDAX Inc., Mahwah, NJ, USA). EDX mappings were performed at a reduced probe current of 1.4 nA in order to reduce impact of sum up and excitation peaks on the line intensity of the evaluated elements. EDX revealed the local sample composition. In order to prove the composition with a higher accuracy and on non-local scale, inductively coupled plasma optical emission spectrometry (ICP OES) measurements were performed after the dissolution of the alloy in aqua regia.

4. Results

Samples with the composition AuCuNiPd, AuCuNiPt, AuCuPdPt, AuNiPdPt, CuNiPdPt and AuCuNiPdPt were prepared and investigated by XRD. As a typical example, the XRD pattern of AuCuNiPt is presented in Figure 1.
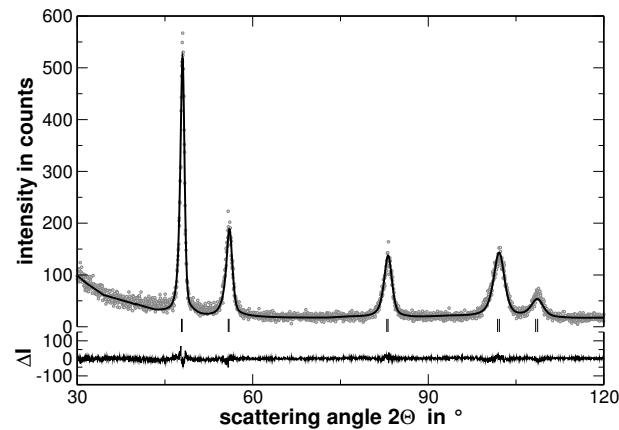
Figure 1. Experimental (points) and calculated (solid line) XRD patterns, as well as their difference ΔI (lower part) of homogenized AuCuNiPt.

The XRD experiments reveal that all samples show a face centered cubic (fcc) structure (The XRD patterns, including the corresponding Rietveld analysis, which are not used for discussion are shown in Appendix A). No traces of secondary phases were detected. Nevertheless, the line broadening is significant even in the homogenized state. This line-broadening, as will be shown in the present article, originates from two major contributions: (i) local lattice strains and (ii) variations of the interplanar spacing, i.e., different lattice parameters, within the sample. The latter originates from segregations. In consequence, and in order to ease the visualization of the effect of segregations on line-broadening, the sample was further heat treated to widen the elemental distribution of the segregation. Before the effect of segregations is displayed, the homogenized state is characterized in the following.

The increase of the background at low scattering angles originates from the silicone grease used to fix the samples and should not be of further interest. The Rietveld analysis revealed that the average lattice parameter of the alloy follows the Vegard's rule of mixture. In order to stress the validation of this rule, the experimentally determined lattice parameter of the samples has been compared to that ones calculated upon the actual sample composition, as shown in Figure 2. Table 1 summarizes the values used. The mean sample composition and its spatial fluctuations were determined by EDX measurements as described in the following.
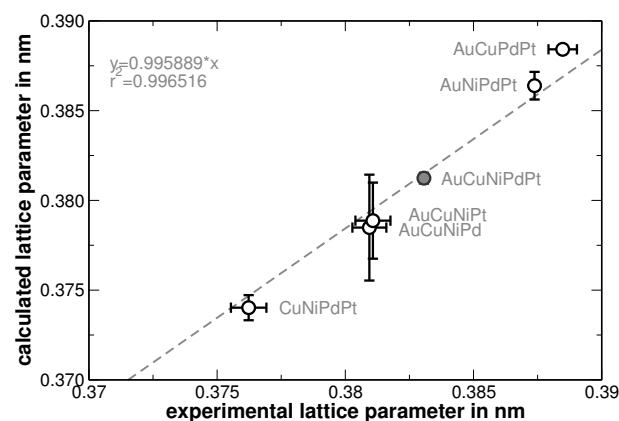

Figure 2. Lattice parameters of the quaternary and quinternary equiatomic solid solutions in the system Au-Cu-Ni-Pd-Pt. The dashed line represents a linear fit to the data.

Table 1. Lattice parameter of the respective fcc structure [18], metallic radius [19] and melting temperature [18] of gold, copper, nickel, palladium and platinum.

Element	Lattice Parameter	Metallic Radius	Melting Temperature
Au	407.82 pm	144 pm	1337 K
Cu	361.49 pm	128 pm	1358 K
Ni	352.40 pm	125 pm	1728 K
Pd	389.07 pm	137 pm	1828 K
Pt	392.42 pm	139 pm	2041 K

The errors depicted for the experimentally determined lattice parameters were taken from the Rietveld analysis, while the errors of the calculated lattice parameters originate from the locally observed variations of the composition as described in the following. The latter errors reflect segregations that have been obtained from a second heat treatment after homogenization. Large segregation was observed for AuCuNiPt. DSC measurements show the onset of melting at $T = 1037\,^\circ$C and a melting range up to $T = 1320\,^\circ$C (the DSC curves are provided in Appendix B). The second heat treatment was performed in the two-phase region above the solidus and below the liquidus temperature in order to promote the formation of segregations. Hence, this sample was heat treated at $T = 1100\,^\circ$C for 17 h and subsequently water-quenched. It turned out that this heat treatment did not alter the spread of the elemental distribution, when compared to the as-cast state. Furthermore, the XRD patterns essentially appeared similar, which is obvious when considering that the measurements were performed on crushed powders. However, the microstructure was coarsened. Heat treatments at lower temperatures, ranging from $T = 600\,^\circ$C to $T = 1000\,^\circ$C were additionally applied. However, these samples do not show this large distribution of concentrations. As expected from DSC measurements, these heat treatments did not result in the formation of secondary phases. When no error bar is shown in Figure 2, the error is smaller than the symbol size. No second heat treatment was applied to the AuCuNiPdPt alloy, therefore, no significant segregations are determined.

An origin for the highly segregated microstructure observed in AuCuNiPd and AuCuNiPt might be connected to sluggish diffusion [20]. According to Table 1 gold atoms have the largest radius among the elements under investigation, while copper and nickel have the smallest radii. The quaternary alloys composed of these three elements (and any fourth one) are expected to show a reduced diffusion rate when compared to alloys composed of atoms with a closer distribution of the metallic radii. In this case, the sluggish diffusion is insufficient to homogenize the highly segregated state. In consequence, the microstructure is comparable to the as-cast state. A wide two-phase (solid + liquid) region might be expected when the melting temperatures of the elements show a large distribution. This could possibly cause large segregations. However, when considering the melting temperatures shown in Table 1, this is not the case.

In order to visualize the effect of the second heat treatment, the high-angle range of the XRD patterns taken on the homogenized as well as on the segregated state of AuCuNiPt is shown in Figure 3. These patterns are cuts from the XRD patterns shown in Figures 1 and 4, respectively. The second heat treatment region affects the XRD line profiles as exemplarily shown in Figure 3 for the 311 and 222 reflections of AuCuNiPt. The shape of the reflections of homogenized samples is of Cauchy type, which turns into a "super Gaussian" type for the segregated sample. The "super Gaussian" line broadening in the segregated state can be interpreted as a convolution of the diffraction lines produced by the homogenized sample with a function describing the distribution of interplanar spacings or local concentrations of individual elements [21].
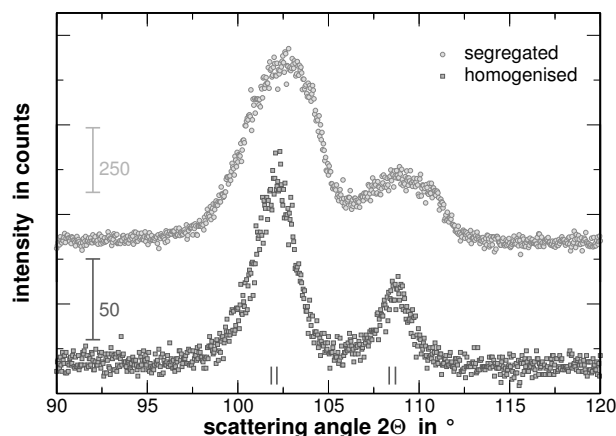
Figure 3. High-angle range of two XRD patterns of AuCuNiPt in the homogenized as well as segregated state. The whole diffraction patterns are shown in Figures 1 and 4.

Multi-component solid solutions with significantly different metallic radii of the constituting elements are expected to cause lattice strains that are reflected by an intense diffuse scattering. In contrast, segregations cause a significant contribution to the width of the reflections determined from XRD experiments, especially if they lead to variations of the interplanar spacing. The latter behavior is demonstrated in Figure 4, where the measured XRD pattern and the corresponding calculated pattern derived by the Rietveld analysis are shown.
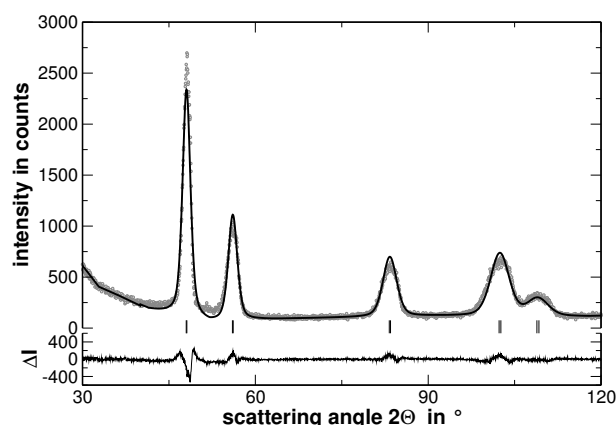

Figure 4. Experimental (points) and calculated (solid line) XRD patterns as well as their difference ΔI (lower part) of AuCuNiPt in a highly segregated state.

Figure 5 shows the microstructure of the AuCuNiPt alloy in a maximum segregated state as well as elemental mapping images obtained from EDX analysis. The SEM micrograph clearly shows a bright area at the grain boundaries and voids, which arise from the annealing in the two-phase region. This sample is heterogeneous, as it was already indicated by the XRD line broadening. However, it contains only a single fcc phase. The elemental mapping images reveal that the copper and gold atoms segregate to the grain boundaries (Figure 5b), which were in the liquid state during annealing at 1100 °C. Furthermore, with respect to the observed distribution of the elements, the grains appear round in shape, which also is interpreted as a consequence of the heat treatment. According to Table 1 Au and Cu have a comparably low melting temperature when compared to the other alloying elements, which is regarded as an origin of the observed behavior. Besides that, the pair mixing enthalpies of binary alloys influence the preferential pairing of particular elements. According to the enthalpies of mixing (as provided in Appendix C) Au-Ni, Cu-Ni and Au-Pt binary bonds are non-preferential in a 1:1 mixture of the elements, while Au-Cu, Ni-Pt and Cu-Pt should be preferred. With the exception of

the binary Cu-Pt bonds, this behavior is also reflected by the observed segregation. The grain boundary is enriched in Au and Cu, i.e., presumably showing a larger number of Au-Cu bonds, and the grain interior is enriched in Ni and Pt, which can be linked to the preference of forming binary Ni-Pt bonds. In addition, Pt has a higher melting temperature than Cu. In consequence, the melt would be rich in Cu and poor in Pt, which is also reflected by the observed elemental distribution shown in Figure 5. Due to this fact, the preference for the Cu-Pt bond cannot be realized and, furthermore, hinders a stronger Cu segregation to the grain boundary in comparison to Au (this is also reflected by Table 2). With the same reasoning, the huge differences in melting intervals between the different alloys as shown in Figure A6 (Appendix B) becomes understandable.
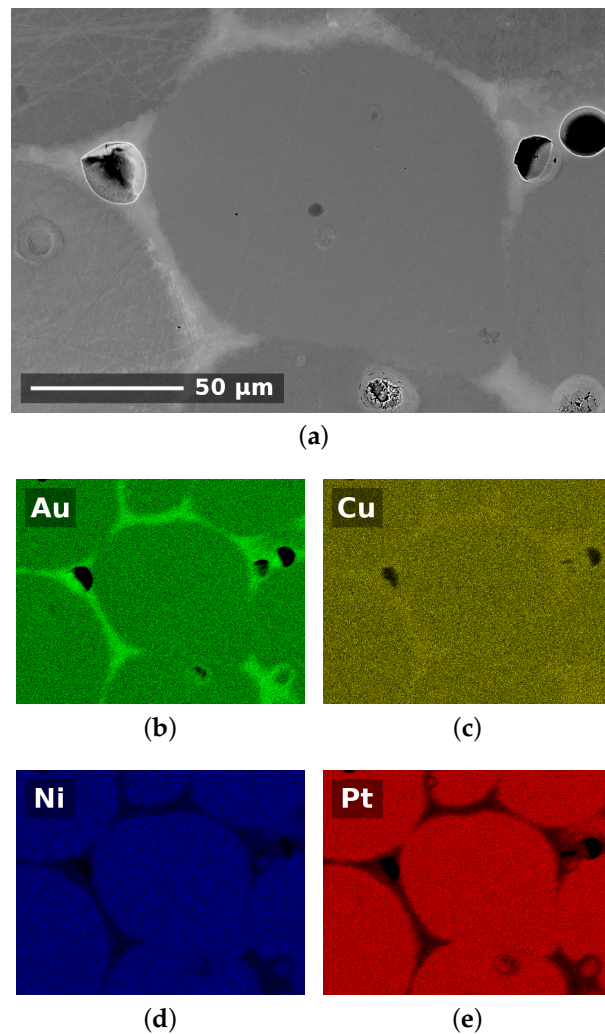
(**a**)

(**b**)

(**c**)

(**d**)

(**e**)

Figure 5. Microstructure (**a**) as obtained from scanning electron microscopy utilizing backscatter electron imaging of AuCuNiPt in the highly segregated state as well as elemental mappings obtained from energy dispersive X-ray analysis (**b**–**e**).

The elemental mappings were not corrected with respect to the atomic number, absorption or fluorescence (ZAF correction). Hence, they are believed to provide qualitative information, only. Nevertheless, this information is further used to evaluate the local elemental distribution of the sample.

The EDX maps were collected with a resolution of 512×400 pixels of which 98.6% were actually considered to provide suitable composition data. The residual pixels are attributed to the voids apparent in Figure 5. The EDX mappings were re-evaluated according to the following scheme. Utilizing the Mathematica software, the four EDX maps had been transferred into a spreadsheet

containing the pixels as well as the colors, which were further processed to the elemental concentration, while zero color saturation equals to zero concentration and maximum color saturation equals to full concentration. For each elemental map, the average value of all pixels under investigation was adjusted to the value obtained from a ZAF corrected areal EDX analysis. The area of this analysis was identical to that of the elemental mappings. The result of this EDX analysis is shown in Table 2. In order to confirm that this local elemental analysis matches the global composition and to demonstrate that it is representative for the whole sample, ICP-OES measurements have been performed. The results are also shown in Table 2. The results proof that the sample preparation does not cause significant (evaporation) losses.

Table 2. Compositions of the sample as obtained on a large scale from ICP-OES measurements (left) as well as obtained locally from EDX analysis covering the whole area shown in Figure 5 and point analyses at the grain interior (dark regions in Figure 5) and the grain boundary (bright regions in Figure 5). The estimated standard deviation was 0.1 at.% for ICP-OES and 1 at.% for EDX, respectively.

Element	Composition			
	ICP-OES	**EDX**	**Grain Interior**	**Grain Boundary**
Au	24.7 at.%	23.6 at.%	19.4 at.%	41.7 at.%
Cu	25.5 at.%	26.7 at.%	20.6 at.%	31.5 at.%
Ni	25.1 at.%	24.2 at.%	31.4 at.%	10.9 at.%
Pt	24.7 at.%	25.5 at.%	28.6 at.%	15.9 at.%

Due to the fact that no correction corresponding adsorption and fluorescence has been applied, the procedure of analyzing the elemental mapping images causes a maximum error of 81%, as the sum of the individual concentrations for each pixel does not sum up to 100%. In order to further evaluate the image, the concentration at each pixel was adapted in a way that the sum of the concentrations at each pixel was normalized to 100%. According to Vegard's rule of mixture, a lattice parameter was assigned to each pixel. The distribution of the lattice parameters obtained from this analysis is of Gaussian type, as shown in Figure 6.
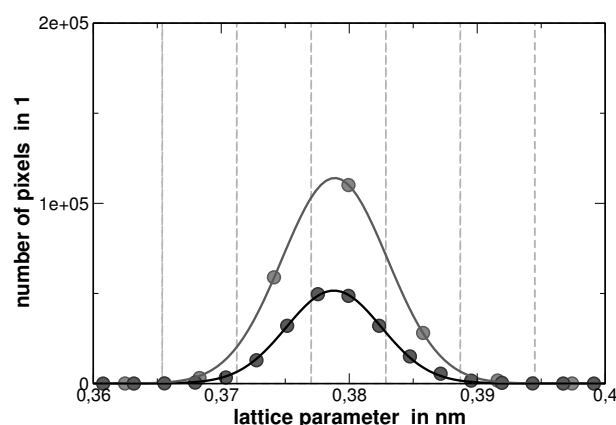

Figure 6. Distribution of the lattice parameters in the segregated sample calculated from the EDX mappings with equidistant separation into 7 and 17 fractions, respectively. The dashed lines in the background indicate the borders corresponding to the separation into 7 fractions.

The center of this distribution matches the experimental lattice parameter. Although there is a large error within the compositions as determined by EDX for the pixels, the error is compensated by the large statistics.

The distribution functions from Figure 6 were employed to fit the experimental XRD profiles by a discrete convolution of Gaussian functions. According to Ref. [22], the discrete convolution can be calculated using:

$$I_i^{\text{calc}} = \sum_j f_j^{(a)} g_{i,j} \qquad (2)$$

In Equation (2), $f_j^{(a)}$ describes the distribution of the lattice parameters normalized to a unity area and $g_{i,j}$ represents the set of mutually shifted Gaussian functions (in a matrix form). Individual functions g_i have their maxima at the Bragg angles that correspond to the respective lattice parameters. I_i^{calc} are the resulting convoluted intensities. To fit the convoluted intensities to the measured ones, the least-squares algorithm was applied. The only refinable parameter was the width of the Gaussian functions.

In order to take the differences in the scattering power of individual atoms into account, the distribution function $f^{(a)}$ was multiplied by a composition-dependent atomic scattering factor, which was obtained from:

$$f(q) = \sum_i m_i \left[\sum_{k=1}^{4} a_{k,i} \exp\left(-b_{k,i} \frac{q^2}{16\pi^2} \right) + c_i \right] \qquad (3)$$

In Equation (3) q represents the scattering vector. The coefficients a_k, b_k and c, which are required to determine the atomic scattering factor are provided in Table A3 in Appendix D. The factors m_i are the molar ratios of individual atomic species. As the convolution from Equation (2) relates to the diffraction angles (and thus to the lattice parameters) but not to the local concentrations, the average concentration of the elements within each fraction classed according to the lattice parameter has been used to calculate the atomic scattering factor for simplicity. An example of the diffraction line 111 fitted by using the above procedure is shown in Figure 7.
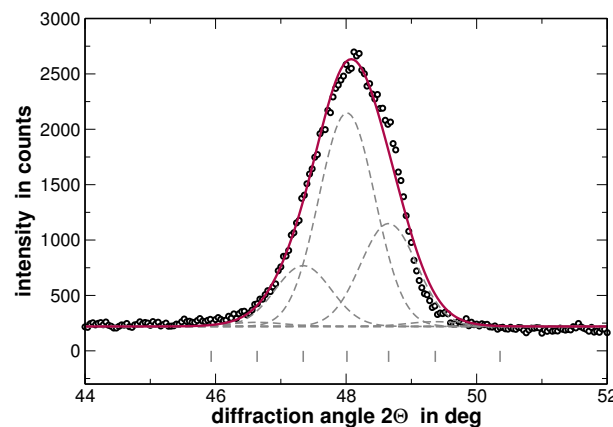

Figure 7. Reflection 111 of AuCuNiPt in the segregated state and seven underlying Gaussian shape reflections of the fractions of which the center positions were indicated. The center positions arise from the average composition within the fractions from which the lattice parameter and in consequence the diffraction angle was calculated.

The results of the fitting procedure are shown in Figure 8. There, the full-width at half-maximum (FWHM) values of the underlying Gaussian profiles are shown for individual diffraction lines and as a function of the fractions used for the line fitting as illustrated in Figure 7. In principle this is the only fitting parameter of interest, since the ratio of the areas of the underlying Gaussian profiles is kept constant (as it is given by the distribution function from Figure 6) and the sum is exclusively fitted.
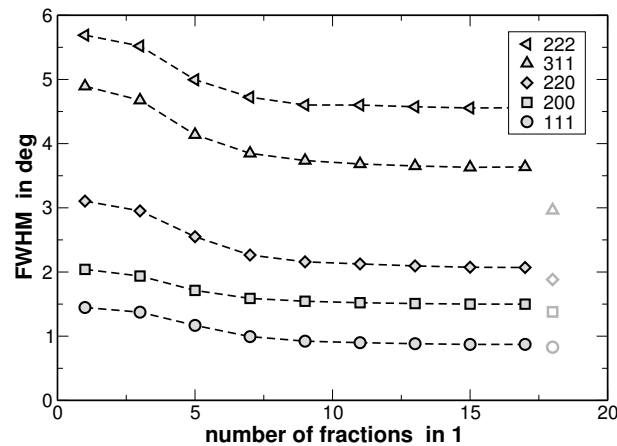
Figure 8. FWHM values of the underlying Gaussian profiles fitted to the labeled reflections of the AuCuNiPt alloy in a highly segregated state in dependence of the number of fractions used for fitting. In addition, the FWHM values obtained from the homogenized state and fitted with a single Gaussian profile are shown (grey symbols).

Figure 8 reveals that the FWHM of the underlying Gaussian profiles decreases with increasing number of fractions and saturates at a nearly constant level if more than 10 fractions are used. It is noteworthy that the FWHM of the main reflections saturate at a value 10%–15% higher than the FWHM value obtained for a sample in the homogenized state (the corresponding values are additionally shown in Figure 8 with grey symbols. The original XRD pattern is presented in Figure 1). The same procedure was applied to the XRD lines of the homogenized state. However, the results do not reveal a significant variation of the FWHM values with increasing number of fractions. This result is explained by the smaller variation of segregations of regions with different lattice parameters in the homogenized state. Furthermore, Figure 8 reveals that the line widths obtained from the fitting are strongly anisotropic, i.e., they depend on the crystallographic direction. Still, this anisotropy of the XRD line broadening could be reproduced by the dependence of FWHM on the cubic invariant $H^2 = (h^2k^2 + k^2l^2 + h^2l^2)/(h^2 + k^2 + l^2)^2$ as described, e.g., by T. Ungár in [23,24]. The values obtained for single profile fitting as well as for fitting with 17 folded profiles were used to perform a modified Williamson-Hall analysis [23–25]. The results are shown in Figure 9.
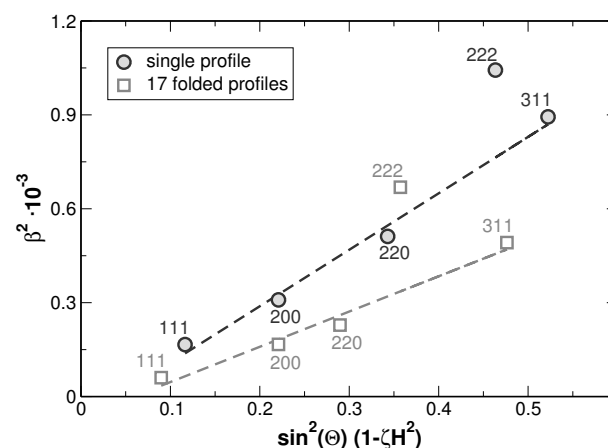

Figure 9. Williamson-Hall analysis of the present results. An alternative presentation of the results, that emphasizes the elastic anisotropy, can be found in Appendix E.

As it can be seen from the modified Williamson-Hall plot, a fitting of the values yields a high goodness of fit as far as the 222 reflections are not considered within the evaluation. This appears

reasonable since the intensities of these reflections are rather low and the 222 reflections show an overlap with the larger neighboring 311 reflections as can be seen from Figure 3. Such anisotropy of the line broadening is typically produced by the anisotropy of elastic constants, when local strain fields are present in the crystalline material. The strain fields can originate either from dislocations or from lattice misfit at the crystallite or grain boundaries. These two effects can be distinguished by employing the effect of the strain on the lattice parameter as shown in [26,27]. The pronounced dependence of the lattice parameters on the crystallographic direction, as shown in Figure 10 indicates that the local lattice strain is produced not only by dislocations but also by a kind of the internal boundaries. Without defects influencing the lattice parameters in specific crystallographic directions, Figure 10 should show a straight extrapolation towards the intercept at $\cos(\Theta)\cot(\Theta) = 0$ and with a slope which is solely depending on the errors of the measurement. Both modified Williamson-Hall plots from Figure 9 revealed that the coherently scattering regions are very large, as it can be expected for the grain sizes in the order of 100 μm (see Figure 5). Additionally, the Williamson-Hall analysis provides values for the lattice strain. The strain values determined from these analyses show (i) large values when compared to homogenized single-element metals and (ii) an apparent enhancement which is attributed to segregations. These were separated to access the true lattice strain. This becomes possible since segregations shift the average lattice parameter, which due to the overlay of different composition appears as line-broadening, while lattice distortions cause an intrinsic line-broadening.
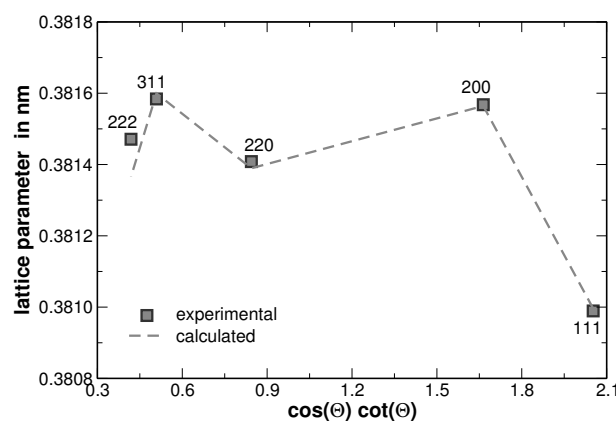

Figure 10. Cohen-Wagner plot for AuCuNiPt in the homogenized state. The corresponding diffraction pattern is shown in Figure 1.

Microscopic lattice strains are commonly defined upon the variation of the interplanar spacing. As the variation of the interplanar spacing is equal to the variation of the lattice parameters in cubic structures the respective microstrain can be written as:

$$e_a = \sqrt{\left\langle \left(\frac{\Delta a}{a}\right)^2 \right\rangle} \qquad \text{and} \qquad e_d = \sqrt{\left\langle \left(\frac{\Delta d}{d}\right)^2 \right\rangle} \tag{4}$$

Commonly, microstrains are assigned to the slope of the Williamson-Hall plot. This slope, is governed by segregations and also influenced by dislocations which was also observed for other systems that obey Vegard's rule of mixture [28–30]. Since, thanks to the EDX measurements, the effect of the lattice parameter variation can be separated from the microstrain. For our samples, the calculation revealed an apparent microstrain due to the concentration fluctuations of 2.3×10^{-2} as determined for 17 fractions upon the distribution shown in Figure 6. The value of the residual microstrain caused by other microstructure defects as obtained from the Williamson-Hall analysis is $(1.5 \pm 0.3) \times 10^{-2}$ for 17 fractions. Without this additional information about the concentration distribution, a Rietveld analysis would not be able to separate these strains, but would reveal an total but partly apparent

microstrain of $e = \sqrt{e_a^2 + e_d^2}$. The Williamson-Hall analysis of the homogenized state yields to a similar value (i.e., $(1.2 \pm 0.1) \times 10^{-2}$) when compared to the analysis of 17 fractions. This value would have been expected when considering the FWHM values observed for 17 fractions in comparison to those of the homogenized state as shown in Figure 8.

5. Discussion

The quaternary AuCuNiPd, AuCuNiPt, AuCuPdPt, AuNiPdPt, CuNiPdPt and the quinternary AuCuNiPdPt equiatomic solid solutions were prepared as single phase solid solutions. Even in case of significant segregations, the alloy crystallizes in a fcc structure. The lattice parameter of these alloys follows the linear rule of mixture between the lattice parameters of the pure elements weighted by their composition.

Segregations can be present in multi-component systems. Due to different diffusion rates of the individual atoms within the matrix, equilibrium conditions might be difficult to obtain. In consequence, the width of X-ray diffraction lines is affected by two major factors: (i) segregations of regions with different lattice parameters and (ii) mesoscopic lattice strains caused possibly by the lattice misfit between the regions with different lattice parameters. The features of the type (i) produce an isotropic spread of the line positions and thus an isotropic XRD line broadening; the mean line positions corresponds to the average lattice parameter. The mesoscopic lattice strains cause both, an anisotropic line broadening and an anisotropic change of the lattice parameters [26,27]. The XRD lines are additionally broadened from dislocations that also originate from the preparation of the powders by filing. However, the microstrain from (homogeneously distributed) dislocations broadens the diffraction lines in an anisotropic manner [23,24], but it does not affect the individual lattice parameters.

The distribution of local chemical compositions was evaluated by EDX analyses. The resulting compositions were converted into lattice parameters by the help of Vegard's rule of mixture. Fractions were defined according to the distribution of the obtained lattice parameters. With varying numbers of defined fractions the profiles of experimental XRD reflections were fitted. The FWHM of the reflections obtained from the fit decreased with increasing number of fractions used for fitting and a saturation behavior has been observed for a number of fractions larger than ten. This behavior indicates that it becomes possible to separate the effect of segregations on the width of XRD reflections. Whenever a large variation in composition within an alloy was observed, a large variation of the lattice parameter was also found, which dramatically broadened the XRD lines. This contribution to the width of the reflection might be the dominant one. As a result, a standard analysis of the XRD line broadening taken into account solely the microstrain will find overestimated results. Instead, the segregations were treated as individual phases with distinct lattice parameters and the same microstrain in order to be able to separate the effects of microstrain and element segregation from each other. As the distribution of the lattice parameter due to segregations and the microstrain broaden the XRD lines in a similar manner (cf. Equation (4)), the distribution of the lattice parameter was determined using the EDX analysis, and only the microstrain was refined from the residual XRD line broadening. However, if the effect of the segregations is less pronounced than that of the lattice strains it will diminish. In this case, i.e., the sample is homogenized, the width of the reflection is dominated by the lattice strains.

6. Conclusions

With AuCuNiPdPt, a novel single-phase high entropy alloy is introduced. The five quaternary equiatomic sub-systems built from these elements have also been shown to be single-phase. Furthermore, the binary and the known ternary sub-systems show a solidification towards a continuous solid solution in the whole concentration range. Hence, it is expected that the region of homogeneity of the alloys presented in this study also covers the whole range of concentrations. This assumption is further supported by the lattice parameter of the alloys following the linear rule of mixture when considering the lattice parameter of the pure elements weighted by their concentration.

Although these alloys are single-phase, the local composition is subjected to segregations. A heat treatment at temperatures in the two-phase region (solid + liquid) promoted the further distribution of these local concentration gradients. This large spread of elemental concentrations was used to investigate its effect on the width of X-ray reflections, as segregations contribute to an increase of the X-ray line width. The segregations were visualized by the help of local element mappings. These EDX maps were quantitatively analyzed, while approved upon the mean concentration matching the overall sample composition. While the division of the concentration spread into several branches yielded to a decrease of the FWHM values of the individual peaks with increasing number of branches, the influence of segregations on the X-ray line width can be detected. As far as segregations of regions with different lattice parameters dominate the width of the X-ray reflections, the FWHM values of the individual peaks decrease. At a large number of branches used for the XRD line profile fitting, the FWHM values of the individual peaks is dominated by other effects. In addition, if segregations are present, the shape of the reflections, as a convolution of the individual peaks, is of the "super Gaussian" type as a rule.

The alloys show a large line-broadening of the XRD reflections also in the homogenized state. Due to the assessment of the artificially-segregated state with the help of multiple underlying peaks, it can be concluded that the large line-broadening of the homogenized samples cannot be governed by segregations, but is caused by residual microstrains.

Author Contributions: Jens Freudenberger designed the experiments, collected and interpreted the data, wrote and edited the article and contributed to all activities. David Rafaja contributed to the text related to XRD and to line profile analysis and fostered the related interpretation. David Geissler and Alexander Kauffmann contributed to scanning electron microscopy, including sample preparation and imaging, they analyzed the results and stimulated their interpretation. Lars Giebeler and Christiane Ullrich contributed to Rietveld analyses. Martin Heilmaier and Kornelius Nielsch directed the research and contributed to the discussion and interpretation of the results.

Conflicts of Interest: The authors declare no conflict of interest.
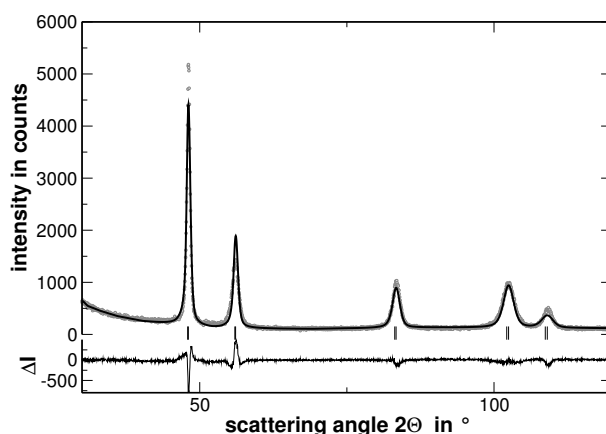
Appendix A. Rietveld Analyses

Figure A1. Experimental (points) and calculated (solid line) XRD patterns as well as their difference ΔI (lower part) and Bragg positions (vertical lines) of homogenized AuCuNiPd.
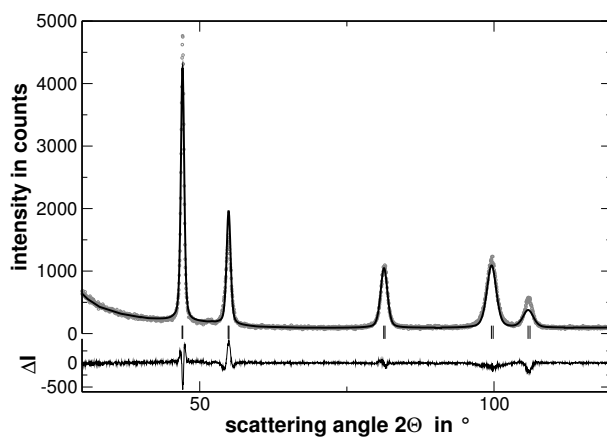
Figure A2. Experimental (points) and calculated (solid line) XRD patterns as well as their difference ΔI (lower part) and Bragg positions (vertical lines) of homogenized AuCuPdPt.

Figure A3. Experimental (points) and calculated (solid line) XRD patterns as well as their difference ΔI (lower part) and Bragg positions (vertical lines) of homogenized AuNiPdPt.
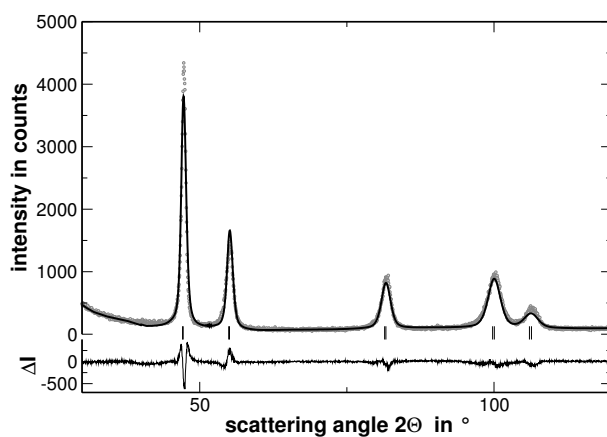

Figure A4. Experimental (points) and calculated (solid line) XRD patterns as well as their difference ΔI (lower part) and Bragg positions (vertical lines) of homogenized CuNiPdPt.

Figure A5. Experimental (points) and calculated (solid line) XRD patterns as well as their difference ΔI (lower part) and Bragg positions (vertical lines) of homogenized AuCuNiPdPt.
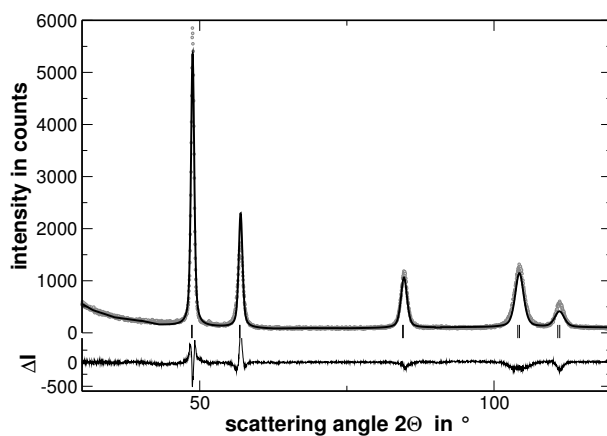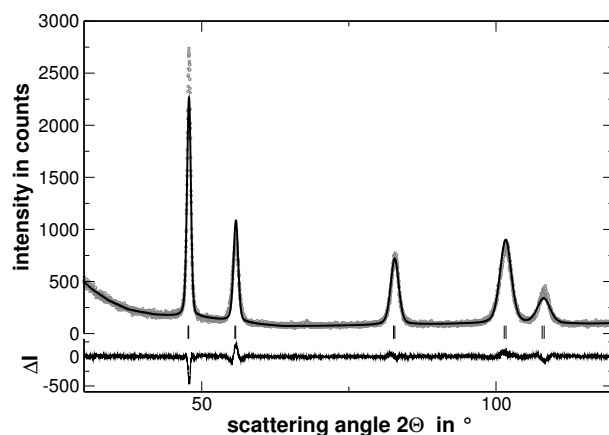
Table A1. Lattice parameters and reliability factors for points with Bragg contributions. Conventional Rietveld R-factors are given using background-corrected counts. Furthermore, the Bragg R-factor and the RF-factor are provided. Values are provided for the homogenized state with the exception of AuCuNiPt *, where the values for the segregated state is given. The R-factors are too large, because the line shape caused by the segregations cannot be described properly. Values for the R-factors are given in per cent.

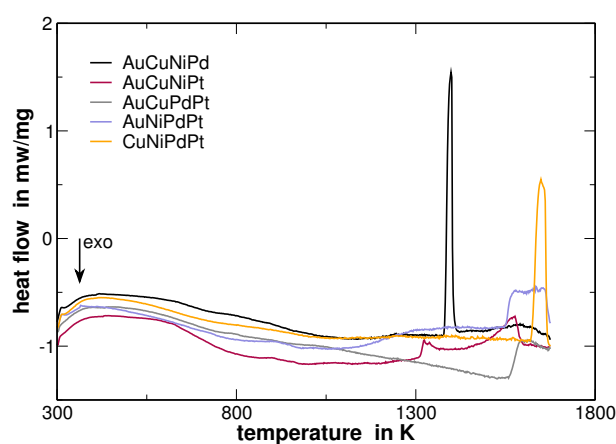| Alloy	Lattice Parameter	R_p	R_{wp}	R_{Bragg}	R_f	χ^2
AuCuNiPd	0.380(93) nm	24.9	22.8	3.99	2.15	3.82
AuCuNiPt	0.381(07) nm	32.6	32.6	8.09	5.64	1.26
AuCuNiPt *	0.381(00) nm	19.8	20.9	7.78	5.15	4.07
AuCuPdPt	0.388(47) nm	23.7	22.6	12.7	8.93	3.94
AuNiPdPt	0.3873(80) nm	20.1	20.8	3.84	2.47	4.16
CuNiPdPt	0.376(22) nm	23.6	22.9	6.99	4.32	4.69
AuCuNiPdPt	0.3830(66) nm	22.0	20.9	7.74	4.90	2.62

Appendix B. DSC Results

Figure A6. DSC (heating curves) of the quaternary alloys.

Appendix C. Pair Mixing Enthalpies

Table A2. Pair mixing enthalpies (in kJ/mol) of binary alloys with equimolar composition. The values were taken from [31].

	Cu	Ni	Pt
Au	−5.2	7.6	5
Cu		2.3	−11.4
Ni			−9.3

Appendix D. Atomic Scattering Factor

Table A3. Equation (3) has been used to estimate the atomic scattering factor. For this purpose the following coefficients were used [32].

Element	a_1	b_1	a_2	b_2	a_3	b_3	a_4	b_4	c
Ni	12.8376	3.8785	7.292	0.2565	4.4438	12.1763	2.38	66.3421	1.0341
Cu	13.338	3.5828	7.1676	0.247	5.6158	11.3966	1.6735	64.8126	1.191
Pd	19.3319	0.698655	15.5017	7.98929	5.29537	25.2052	0.605844	76.8986	5.26593
Pt	27.0059	1.51293	17.7639	8.81174	15.7131	0.424593	5.7837	38.6103	11.6883
Au	16.8819	0.4611	18.5913	8.6216	25.5582	1.4826	5.86	36.3956	12.0658

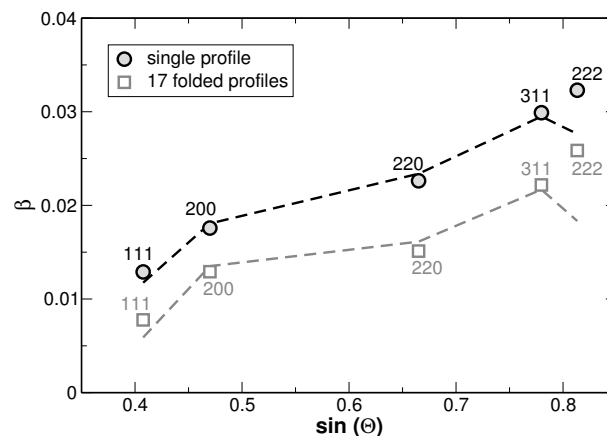## Appendix E. Modified Williamson-Hall Plot

Figure A7. Alternative view of the Williamson-Hall analysis shown in Figure 9, pronouncing the elastic anisotropy of the XRD line broadening. The dashed lines represent fits to the line broadening including the cubic invariant according to References [23,24].

References

1. Cantor, B.; Chang, I.T.H.; Knight, P.; Vincent, A.J.B. Microstructural development in equiatomic multicomponent alloys. *Mater. Sci. Eng. A* **2004**, *375–377*, 213–218.

2. Ye, Y.F.; Wang, Q.; Lu, J.; Liu, C.T.; Yang, Y. High-entropy alloy: Challenges and prospects. *Mater. Today* **2016**, *19*, 349–362.

3. Ruiz-Yi, B.; Bunn, J.K.; Stasak, D.; Mehta, A.; Besser, M.; Kramer, M.J.; Takeuchi, I.; Hattrick-Simpers, J. The Different Roles of Entropy and Solubility in High Entropy Alloy Stability. *ACS Comb. Sci.* **2016**, *18*, 596–603.

4. Yeh, J.-W.; Chen, S.-K.; Lin, S.-J.; Gan, J.-Y.; Chin, T.-S.; Shun, T.-T.; Tsau, C.-H.; Chang, S.-Y. Nanostructured High-Entropy Alloys with Multiple Principal Elements: Novel Alloy Design Concepts and Outcomes. *Adv. Eng. Mater.* **2004**, *6*, 299–303.

5.   Tsai, M.-H.; Yeh, J.-W. High-Entropy Alloys: A Critical Review. *Mater. Res. Lett.* **2014**, *2*, 107–123.

6.   Zhang, Y.; Zuo, T.T.; Tang, Z.; Gao, M.C.; Dahmen, K.A.; Liaw, P.K.; Lu Z.P. Microstructures and properties of high-entropy alloys. *Prog. Mater. Sci.* **2014**, *61*, 1–93.

7.   Miracle, D.B.; Senkov, O.N. A critical review of high entropy alloys and related concepts. *Acta Mater.* **2016**, *122*, 448–551.

8.   Kozak, R.; Sologubenko, A.; Steurer, W. Singe-phase high-entropy alloys—An overview. *Z. Kristallogr.* **2015**, *230*, 55–68.

9.   Youssef, K.M.; Zaddach, A.J.; Niu, C.; Irving, D.L.; Koch, C.C. A Novel Low-Density, High-Hardness, High-entropy Alloy with Close-packed Single-phase Nanocrystalline Structures. *Mater. Res. Lett.* **2014**, *3*, 95–99.

10. Zhang, C.; Zhang, F.; Diao, H.; Gao, M.C.; Tang, Z.; Poplawsky, J.D.; Liaw, P.K. Understanding phase stability of Al-Co-Cr-Fe-Ni high entropy alloys. *Mater. Des.* **2016**, *109*, 425–433.

11. Song, H.; Tian, F.; Wang, D. Thermodynamic properties of refractory high entropy alloys. *J. Alloys Compd.* **2016**, *682*, 773–777.

12. Senkov, O.N.; Wilks, G.B.; Miracle, D.B.; Chuang, C.P.; Liaw, P.K. Refractory high-entropy alloys. *Intermetallics* **2010**, *18*, 1758–1765.

13. Feuerbacher, M.; Heidelmann, M.; Thomas, C. Hexagonal High-entropy Alloys. *Mater. Res. Lett.* **2015**, *3*, 1–6.

14. Villars, P. SpringerMaterials Au-Ni Binary Phase Diagram 0–100 at.% Ni. Available online: http://materials.springer.com/isp/phase-diagram/docs/c_0906519 (accessed on 2 September 2016).

15. Maiti, S.; Steurer, W. Structural-disorder and its effect on mechanical properties in single-phase TaNbHfZr high-entropy alloy. *Acta Mater.* **2016**, *106*, 87–97.

16. Rietveld, H.M. A Profile Refinement Method for Nuclear and Magnetic Structures. *J. Appl. Cryst.* **1969**, *2*, 65–71.

17. Rodriguez-Carvajal, J. Recent advances in magnetic structure determination by neutron powder diffraction. *Physica B* **1993**, *192*, 55–69.

18. The Periodic Table by WebElements. Available online: http://www.webelements.com (accessed on 27 November 2016).

19. Wells, A.F. *Structural Inorganic Chemistry*, 5th ed.; Clarendon Press: Oxford, UK, 1984.

20. Pickering, E.J.; Jones, N.G. High-entropy alloys: A critical assessment of their founding principles and future prospects. *Int. Mater. Rev.* **2016**, *61*, 183–202.

21. Rafaja, D.; Dopita, M.; Masimov, M.; Klemm, V.; Wendt, N.; Lengauer, W. Analysis of local composition gradients in the hard-phase grains of cermets using a combination of X-ray diffraction and electron microscopy. *Int. J. Refract. Met. Hard Mater.* **2008**, *26*, 263–275.

22. Rafaja, D. Deconvolution versus convolution—A comparison for materials with concentration gradient. *Mater. Struct.* **2000**, *7*, 43–50.

23. Ungár, T.; Dragomir, I.; Revesz, A.; Borbély, A. The contrast factors of dislocations in cubic crystals: The dislocation model of strain anisotropy in practice. *J. Appl. Cryst.* **1999**, *32*, 992–1002.

24. Ungár, T. Microstructural parameters from X-ray diffraction peak broadening. *Scr. Mater.* **2004**, *51*, 777–781.

25. Williamson, G.K.; Hall, W.H. X-ray line broadening from filed aluminium and wolfram. *Acta Metall.* **1953**, *1*, 22–31.

26. Šimek, D.; Rafaja, D.; Motylenko, M.; Klemm, V.; Schreiber, G.; Brethfeld, A.; Lehmann, G. XRD analysis of local strain fields in pearlitic steels—Towards the fast examination of microstructure after rolling. *Steel Res. Int.* **2008**, *79*, 800–806.

27. Šimek, D.; Oswald, A.; Schmidtchen, R.; Motylenko, M.; Lehmann, G.; Rafaja, D. Prediction of Mechanical Properties of Carbon Steels After Hot and Cold Forming by Means of Fast Microstructure Analysis. *Steel Res. Int.* **2014**, *85*, 1369–1378.

28. Wüstefeld, C.; Rafaja, D.; Dopita, M.; Motylenko, M.; Baehtz, C.; Michotte, C.; Kathrein, M. Decomposition kinetics in $Ti_{1-x}Al_xN$ coatings as studied by in-situ X-ray diffraction during annealing. *Surf. Coat. Technol.* **2011**, *206*, 1727–1734.

29. Rafaja, D.; Wüstefeld, C.; Baehtz, C.; Klemm, V.; Dopita, M.; Motylenko, M.; Michotte, C.; Kathrein, M. Effect of internal interfaces on hardness and thermal stability of nanocrystalline $Ti_{0.5}Al_{0.5}N$ coatings. *Metall. Mater. Trans. A* **2011**, *42*, 559–569.

30. Rafaja, D.; Wüstefeld, C.; Dopita, M.; Motylenko, M.; Baehtz, C. Capability of X-ray diffraction for the study of microstructure of metastable thin films. *IUCrJ* **2014**, *1*, 446–456.

31. The Landolt Börnstein Database. Available online: http://materials.springer.com (accessed on 2 September 2016).

32. Prince, E. (Ed.) *International Tables for Crystallography: Mathematical, Physical and Chemical Tables*; International Union of Crystallography: Chester, UK, 2006; Volume C.